Surface modification effect on contrast agent efficiency for X-ray based spectral photon-counting scanner/luminescence imaging: from fundamental study to in vivo proof of concept

Loic Cuau, Pia Akl, Arthur Gautheron, Angèle Houmeau, Fréderic Chaput, Ala Yaromina, Ludwig Dubois, Philippe Lambin, Szilvia Karpati, Stephane Parola, et al.

Surface modification effect on contrast agent efficiency for X-rays based Spectral Photon-Counting Scanner / Luminescence Imaging: from fundamental study to in vivo proof of concept.

Loic Cuau[a], Pia Akl[b,c], A Gautheron[b,d], Angèle Houmeau[b], Frédéric Chaput[a], Ala Yaromina[e], Ludwig Dubois[e], Philippe Lambin[e], Szilvia Karpati[a], Stephane Parola[a], Jean-Baptiste Langlois[f], Yoad Yagil[g], Salim A. Si-Mohamed[b,c], Bruno Montcel[b], Philippe Douek[b,c], Frederic Lerouge[a]*

a Université de Lyon, Ecole Normale Supérieure de Lyon, CNRS UMR 5182, Université Claude Bernard Lyon 1, Laboratoire de Chimie, 46 allée d'Italie, F69364 Lyon, France

b Université de Lyon, INSA-Lyon, Université Claude Bernard Lyon 1, UJM-Saint Etienne ,CNRS , Inserm, CREATIS UMR 5220, U1294, F-69621, LYON, France.

c Department of Radiology, Hospices Civils de Lyon, 69500 Bron, France.

d Université Jean Monnet Saint-Etienne, CNRS, Institut d'Optique Graduate School, Laboratoire Hubert Curien UMR 5516, F-42023, SAINT-ETIENNE, France

e Department of Precision Medicine, The M-Lab, GROW – School of Oncology, Maastricht University, Maastricht, 6200, MD, The Netherlands.

f CERMEP-imagerie du vivant, 59 boulevard Pinel, 69500 Bron

g Global Advanced Technologies, CT, Philips, Haifa, Israel

** corresponding author*

Abstract

X-Rays imaging techniques are among the most widely used in medical imaging and their constant evolution has led to the emergence of new technologies. The new generation of computed tomography (CT) systems: spectral photonic counting CT (SPCCT) and X-Rays luminescence optical imaging are examples of such powerful techniques. With these new technologies the rising demand for new contrast agents has led to extensive research in the field of nanoparticles and the possibility to merge the modalities appears to be highly attractive. In this work, we propose the design of lanthanide-based nanocrystals as multimodal contrast agent with the two aforementioned technologies, allowing SPCCT and optical imaging at the same time. We present a systematic study on the effect of Tb^{3+} doping level and surface modification on the generation of contrast with SPCCT and the luminescence properties of GdF_3:Tb^{3+} nanocrystals (NCs), comparing different surface grafting with organic ligands and coatings with silica to make these NCs bio-compatible. A comparison of the luminescence properties of these NCs with UV revealed that the best results were obtained for the $Gd_{0.9}Tb_{0.1}F_3$ composition. This property was confirmed under X-Rays excitation in microCT as well as with SPCCT. Moreover, we could demonstrate that the intensity of the luminescence as well as the excited state lifetime are strongly affected by the surface

modification. On the other side, whatever the chemical nature of the ligand, the contrast with SPCCT did not change. Finally, the successful proof of concept of multimodal imaging was performed in vivo with nude mice in the SPCCT taking advantage of the so-called color k-edge imaging method.

Introduction

The development of original and efficient nanoparticle-based contrast agents represents a significant part of the ongoing improvement in medical imaging. The constant advances in the field of nanotechnologies play a major role in offering new tools for enhanced and optimized imaging with great potential for clinical applications.[1] Among the existing modalities, X-Rays imaging techniques are most commonly used owing to their fast acquisition, high spatial resolution and low cost, which make them extremely relevant for clinics. A typical example is computed tomography (CT), which has become a widely used clinical X-Rays imaging modality since its first development fifty years ago. In addition, other techniques such as X-rays micro-CT have received growing interest in life science imaging and preclinical studies on small animals thanks to their higher resolution.[2,3] Constant developments of these X-Rays imaging modalities have led to many newly emerging technologies such as the recent color K-edge imaging that have been deployed on spectral photon-counting CT (SPCCT).[4-6] This new generation of CT systems combines high resolution (250 μm), element-specific imaging as well as *in situ* quantification.[7,8] One issue still remains to be addressed due to the intrinsic X-Rays absorption in normal tissues that leads to relatively low imaging sensitivity. Recently, X-Rays-activated luminescence has been considered as promising approach for high sensitivity and deep-tissue imaging.[9,10] Indeed, the combination of X-Rays excitation and visible luminescence combines successfully the strengths of both techniques: deep tissue penetration, low X-Rays scattering in tissue, and negligible auto-fluorescence background.[11]

The improvement of these techniques (CT, SPCCT and X-ray activated luminescence) is strongly related to the elaboration of novel X-ray sensitive contrast agents.[12,13] Thus, intensive research has been proposed on the development of inorganic nanoparticles to improve contrast with the new SPCCT imaging modality[14] or the optimization of luminescent nanoparticles for X-rays excited optical imaging.[9,15] Unfortunately, very few studies propose the design of nanoparticles acting as innovative contrast agents for the effective combination of both X-ray based modalities.[16-18] Indeed the possibility to bring together CT, SPCCT and X-ray activated optical imaging with the same nanoparticle-based

contrast agent offers a great interest for the development of multimodal imaging with strong impacts on the future of diagnostic.

Within the toolbox of available nanoparticles, compositions sometimes include elements with high toxicity such as tungsten or chromium which despite good luminescence properties limits their interest for further use in vivo.[17,19] Lanthanide-based rare earth sodium fluoride nanoparticles $NaREF_4$ are interesting systems featuring all the essential characteristics that make them ideal candidates with heavy elements, attractive optical properties with narrow emission bands and excellent photostability.[20,21] The only weakness of these nanoparticles is their limited chemical stability in aqueous suspensions (pure water and buffers at pH 7.7 and 8.0) or under neutral physiological conditions.[22-24]

In this context, the aim of our work was to design multimodal contrast agents suitable for X-Rays based imaging technologies with high colloidal stability and biocompatibility. Recently, we demonstrated that GdF_3 nanocrystals (NCs) are efficient systems for in vivo imaging with SPCCT due to their X-Rays attenuation properties.[25] Indeed, gadolinium has a K-edge value in a range of energy perfectly suited for K-edge imaging with SPCCT technology (50,2 keV).[26,27] Furthermore, this element is already used for MRI in clinics or in nanoparticles research developments.[28] Also, due to its very low solubility in aqueous media (less than 3.10^{-5} mol L^{-1}), GdF_3 can be considered as one of the most stable gadolinium derivatives, making it the matrix of choice for this work.[29] The rational design of the targeted nanoparticles for X-rays imaging technologies requires a comprehensive understanding of the parameters inducing optimized luminescence, contrast with scanner and biocompatibility. Hence, in order to provide luminescence X-Rays activation properties, the GdF_3 matrix was doped with various amounts of Tb^{3+} (from 0,20 molar to 0,05 molar). A systematic study using UV/Vis and X-rays irradiation identified the most relevant composition in terms of luminescence intensity and emission lifetime. For water dispersibility NCs were functionalized with various ligands and coatings including polyacrylic acid, sodium tripolyphosphate, polyethylene glycol bearing phosphonic acid function and silica layer. Nevertheless, it is known that the presence of surface-linked molecules (e.g., C–H, O–H vibrational modes of ligands) or hydroxyl groups in aqueous media can act as luminescence quenchers.[30,31] This motivated to study the luminescence behavior of NCs surface modified with the typical ligands and coating, expanding the knowledge of water dispersible X-Rays activated nano-contrast agents properties. Finally, the interest and feasibility to use optimal systems for multimodal imaging in vivo

were illustrated through a proof of concept with nude mice, upon X-Rays activation in the SPCCT using a clinical sequence aquisition.

Experimental

Synthesis of NCs of various compositions

The typical procedure for the $Gd_{0,80}Tb_{0,20}F_3$ composition is as follow (quantities are then adapted for other compositions) : A solution consisting in $GdCl_3$, 6 H_2O (3.87 g, 9.8 mmol) and $TbCl_3$, 6 H_2O (0.21 g, 1.1 mmol) dissolved in ethylene glycol is added with a solution of hydrofluoric acid (875 µL, aqueous solution 50% by mass) in with 2-pyrrolidinone. The transparent mixture is placed in a Teflon insert and then heated in an autoclave at 170° C for 1 hour. The light brown product is treated with acetone to precipitate the nanoparticles. After purification steps by centrifugation-redispersion cycles in methanol the particles are finally dispersed in ultrapure water to give a transparent suspension.

Surface modification of NPs with various ligands

$Gd_{0,90}Tb_{0,10}F_3$@PEG : A solution of 7.7 g ($7.7x10^{-3}$ mol, 0.3 eq.) of PEG phosphonic acid in water is added on 50g of a colloidal suspension of NPs (10% w/w). The mixture is heated at 80°C overnight under stirring and purified by dialysis. The final product is freeze dried and kept at solid state.

$Gd_{0,90}Tb_{0,10}F_3$@PAA : A solution of 0.99 g ($4.95X10^{-4}$ mol, 0.04 eq.) of PAA in NaOH (0.1M) is added on 30 g of a colloidal suspension of NPs (10% w/w). The mixture is heated at 80°C under vigorous stirring. After purification by dialysis, the final product is freeze-dried.

$Gd_{0,90}Tb_{0,10}F_3$@TPP : A solution of 0.38 g ($8.16x10^{-4}$ mol, 0.59 eq.) of TPP in water is added on 0,3 g of NPs in water. The mixture is heated at 80°C under stirring. After purification by dialysis, the final product is freeze-dried.

$Gd_{0,90}Tb_{0,10}F_3$@SiO_2@PEG : The preparation of the surface-modified nanoparticles follows 3 main steps : 1/ ($Gd_{0.90}Tb_{0.10}F_3$@*silicate*) 20.8 mL of a solution of sodium silicate (3% w/w) are added on 50 g of a suspension of nanoparticles (10% w/w) under stirring. The mixture is heated for 1 hour at 80°C and purified by dialysis. 2/ ($Gd_{0.90}Tb_{0.10}F_3$@SiO_2) 1g of the previously prepared nanoparticle is suspended in water ($92mg.mL^{-1}$) and added to a solution consisting of 11.7 mL water, 3150 µL ethanol and 114 µL ammoniac. A solution of TetraEthylOrthoSilicate (TEOS) in ethanol (841.6 µL, $3.80x10^{-3}$ mol, in 1245 µL EtOH) is partially added in 4 steps every hour. After the last addition the mixture is stirred 45 min at

room temperature and purified by dialysis. 3/ A suspension of the previously prepared $Gd_{0.90}Tb_{0.10}F_3@SiO_2$ in water (500mg, 20 mL) is mixed with a solution of 1.52 mL ethanol, 154 µL ammoniac and 750 mg of PEG silane (Mw 2000) during 24 hours under vigorous stirring. The final colloidal suspension is purified by dialysis and the particles are freeze-dried.

Analysis of particle morphology and composition

DLS and Zeta potential measurements were performed on liquid suspensions of the nanoparticles, using a Malvern Instruments Nano ZS. TEM images were acquired using a JEOL 2100F and operated at 120kV. TGA analysis were performed on a setaram LABSYS1600. FTIR spectra were recorded on a Perkin Elmer Spectrum 65 equipped with an ATR module.

Luminescence and lifetime measurements

The emission spectra of the NCs were measured using a Horiba-Jobin-Yvon Fluorolog-3 fluorimeter using a system of three monochromatic double-grid slits. The luminescence ground state was excited by unpolarized light emitted by a 450 W continuous xenon lamp. The spectra were plotted by correcting the spectrum of the lamp and that of the detector. For the terbium (III) doped samples the entrance and exit slits were set to a 2 nm width. In all cases, the integration time used was 0.1s. Decay in luminescence was obtained using an FL-1040P pulsed xenon lamp and half-life times were calculated by exponential fit using Origin® software.

Scintillation studies on micro-CT

Irradiation and imaging were performed using an X-RAD225Cx device (Precision X-Ray, North Brandford, CT) equipped with a copper X-ray tube and a tungsten anode with an aluminum filter. The irradiated samples are contained in quartz tanks. Scintillation was detected by a camera positioned vertically to the tank at an angle of 90° to the source in order to acquire maximum luminescence.

Scintillation studies on SPCCT

SPCCT-induced Luminescence measurements were performed using an experimental setup composed of an immersed optical fiber connected to a spectrometer. In addition, a homemade electronic circuit triggers the spectrometer with the X-ray emission. The cleaved end of the optical fiber (FG550UEC Thorlabs Inc.) was immersed in the nanoparticle solution and the SMA connector end was connected to the spectrometer via a round-to-Linear bundle of fiber (PL200-2-VIS-NIR, Ocean Insight). The bundle maximizes the light signal entering the spectrometer (Ocean Insight MayaPro2000). The spectrometer has previously been calibrated in order to give absolute spectral irradiance measurements. The

luminescence measurements were triggered by a dedicated electronic circuit that detects the excitation X-Ray signal emitted from the SPCCT using a stand-alone X-Ray detector (Philips). The detector is composed of a basic scintillation detector attached to a photodiode encapsulated in epoxy to protect the assembly. The trigger circuit is composed of 4 electronic stages for amplifying the detector signal which is wired to an input pin of the Arduino Board, which is required to generate a TTL signal. The TTL signal is then fed to the triggering pin of the spectrometer. The trigger circuit allowed us to measure the light spectra both during excitation (X-Ray on) and background (X-Ray off). The luminescence spectrum is obtained by subtracting the background spectrum from the excitation spectrum. This suppresses any background parasitic light that could impair the luminescence emission. Finally, we applied a sliding average filtering with a window of 3 pixels to reduce the noise.

***in vivo* experiment**

A Nude Swiss female mouse used for the in vivo studies was purchased from Charles River Laboratories (7 weeks old) weighing about 30-35 g. The animal was provided with standard mouse food and water ad libitum and maintained under conventional housing conditions in a temperature-controlled room with 12-hour dark–light cycle. All experiments were carried out in accordance with the European Directive 2010/63/UE, approved by the Ethics Committee (CELYNE CEEA42) and authorized by the Ministry of Higher Education, Research and Innovation (APAFIS#19829).

Results and Discussion

Design and Characterization of the NCs.

The four compositions of NCs were prepared under solvothermal conditions, following a previously described process with some modifications.[32] Briefly, the desired amounts of rare earth salts of Gd^{3+} and of Tb^{3+} (with respective molar ratios 0.95/0.5; 0.90/0.10; 0.85/0.15 and 0.80/0.20) in ethylene glycol were reacted with a charge transfer complex involving F^- anions and protonated pyrrolidinone. The mixture was heated in an autoclave for 1 hour and purified by centrifugation/redispersion steps to finally give a clear, colorless suspension of nanoparticles in water.

Powder X-ray Diffraction (PXRD) confirmed that all samples have a highly crystalline structure with a GdF_3 orthorhombic phase (Pnma space group, lattice parameters: a = 6.5710 Å , b = 6.9850 Å , c = 4.3930 Å and $\alpha = \beta = \gamma = 90°$) when compared to ICDD 00-049-1804 theoretical pattern (Fig. 1A – Fig. S1). The composition of the prepared systems was determined by elemental analysis (Inductively Coupled

Plasma – ICP) confirming that for all four compositions, the ratio between Gd^{3+} and Tb^{3+} in the inorganic core was consistent with what was expected for the synthesis (Table S2).

The size and morphology of nanoparticles were characterized by transmission electron microscopy (TEM) and dynamic light scattering (DLS). Whatever the composition, the NCs show slightly elongated morphologies ("bean-like") with a 9.8 ± 0.8 nm average gyration diameter (Fig. 1B).

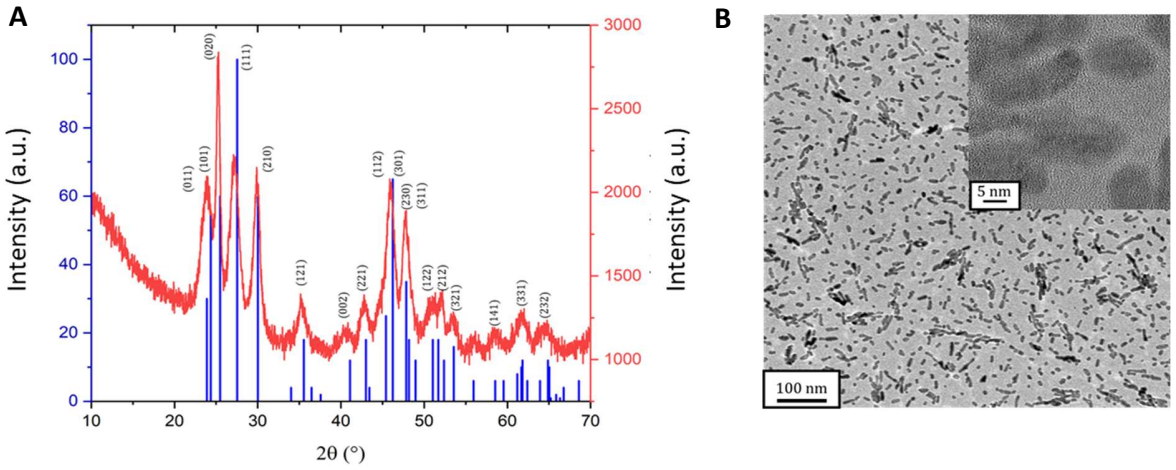

C

Composition	Crystallographic Structure	Average diameter (nm)
$Gd_{0.95}Tb_{0.05}F_3$	GdF_3 orthorhombic	10.1 ± 0.8
$Gd_{0.90}Tb_{0.10}F_3$	GdF_3 orthorhombic	9.8 ± 0.8
$Gd_{0.85}Tb_{0.15}F_3$	GdF_3 orthorhombic	9.5 ± 0.8
$Gd_{0.80}Tb_{0.20}F_3$	GdF_3 orthorhombic	9.1 ± 0.8

Fig. 1 A) PXRD of $Gd_{0.95}Tb_{0.05}F_3$ (red line) compared with ICDD 00-049-1804 theoretical pattern (blue lines). **B)** TEM image of NCs. HRTEM of the same sample in the inset. **C)** Results of the PXRD and TEM results for all compositions

DLS measurements in water showed a low polydispersity of NCs and hydrodynamic diameters in the 13-18 ± 3 nm range (Table S3). These results confirm that the amount of terbium added did not affect the size, the morphology nor the crystallinity of the desired nanocrystals. Zeta potential measurements in water (pH 6) gave positive values of 48 ± 2 mV, whatever the composition, confirming the high colloidal stability of these systems. The positive charge can be explained by the excess of lanthanide ions on the surface in accordance with energy dispersive X-ray spectroscopy analysis (Fig. S4).

Fourier-transform infrared spectroscopy (ATR-FTIR) analysis shows specific bands of remaining 2-pyrolidinone molecules on the surface of the particles as previously observed.[33] Upon coordination through the oxygen atom of the carbonyl bond, the C=O stretching vibration frequency of 2-pyrrolidinone shifts from 1679 cm^{-1} to 1648 cm^{-1}. The bands of the molecule in the range 1463-1424 cm^{-1} can be attributed to C-H deformations and they are shifted to 1448 cm^{-1} once on the NPs. Finally, the C-N vibration of the 2-pyrrolidinone cycle, initially observed at 1284 cm^{-1}, shifts to 1313 cm^{-1} suggesting interactions between the nitrogen atoms and lanthanides on the surface of the particles.

Optical properties of the NCs

The luminescence properties of the NCs were first studied upon excitation at 273 nm, in water (0.30 M in Lanthanides). This wavelength corresponds to the transition between the energy levels $^8S_{7/2}$ and ^6I_J of Gd^{3+} (Fig. 2).[34]

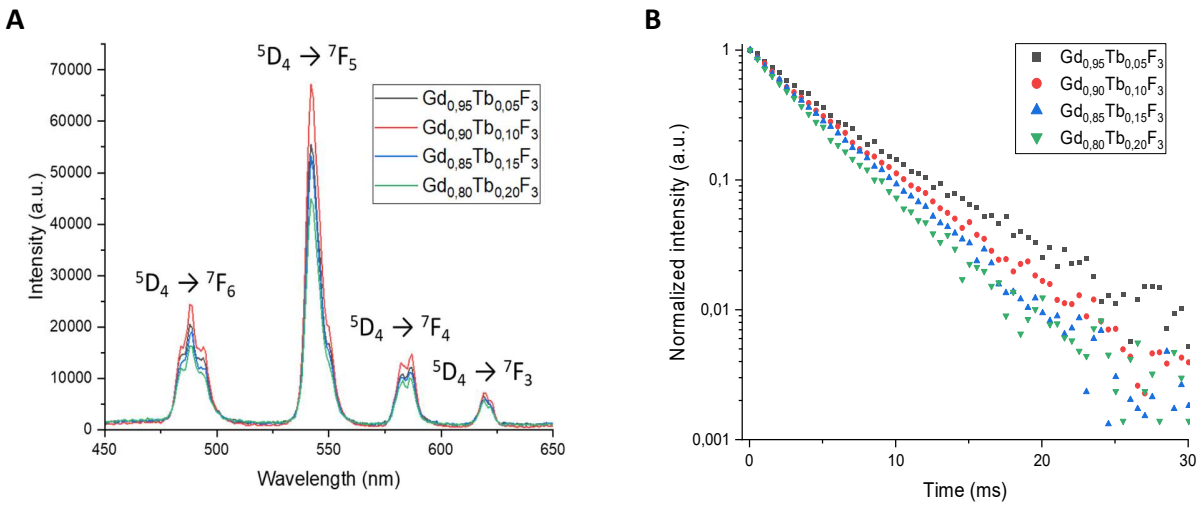

Fig. 2 A) Luminescence spectra of the various NCs compositions after excitation at 273nm. **B)** Lifetime decay measurements after excitation at 273 nm.

For all cases, the emission spectra observed are characteristic of Tb^{3+} and the bands centered at 488 nm, 543 nm, 582 nm and 619 nm correspond to the energy transition from $^5D_4$ to ^7F_J (J = 6,5,4,3).[35] The maximum luminescence intensity is observed for the $Gd_{0.90}Tb_{0.10}F_3$ composition and other systems show lower intensities independently of Tb^{3+} amount. Furthermore, when the molar ratio of Tb^{3+} increases above 0.10 the luminescence decreases. This result can be explained by the interactions between Tb^{3+} in excited states. When the ions are in close vicinity within the NPs matrix, phenomenon such as reabsorption and non-radiative deexcitations lead to the quenching of luminescence. To further

confirm optimum wavelength of excitation, spectra of the $Gd_{0.90}Tb_{0.10}F_3$ composition were recorded at each emission band of Tb^{3+} (i.e 488 nm, 543 nm, 582 nm, 619 nm). Whatever the Tb^{3+} band considered, the excitation spectra show an intense signal centered at 273 nm (Fig. S5). This corresponds to the transition of the energy level of the Gd^{3+} present in the crystalline matrix ($^8S_{7/2}$ to ^6I_J), proving that the emission of the NCs results from an energy transfer from Gd^{3+} to Tb^{3+}.

Measurements of the luminescent decay of each composition were conducted at 543 nm with an excitation wavelength at 273 nm. The decays fit well with a monoexponential rate and respective fluorescence lifetimes have been evaluated for the different ratio Gd^{3+}/Tb^{3+} (Table 1).

Table 1 Luminescence lifetime of each composition at 543 nm with an excitation wavelength at 273 nm and a concentration of 0.3M in water.

Composition	*Lifetime (ms)*	*Coorelation coefficient*
$Gd_{0.95}Tb_{0.05}F_3$	4.30 ± 0.04	0.998
$Gd_{0.90}Tb_{0.10}F_3$	4.84 ± 0.04	0.998
$Gd_{0.85}Tb_{0.15}F_3$	4.04 ± 0.03	0.998
$Gd_{0.80}Tb_{0.20}F_3$	3.57 ± 0.03	0.998

All lifetime values are in the 4.04 – 4.84 ms range except for the $Gd_{0.80}Tb_{0.20}F_3$ composition with 3.57 ms. The lifetimes results follow the trend observed with luminescence intensity and a maximum is measured for an optimal molar amount of Tb^{3+}. Indeed, the $Gd_{0.90}Tb_{0.10}F_3$ composition shows both the highest luminescence lifetime (4.84 ms) as well as the highest intensity. As lifetime can be directly linked to photoluminescence quantum yield,[36] the $Gd_{0.90}Tb_{0.10}F_3$ NPs seem to present the most interesting optical properties, and this composition will be the candidate of choice for further studies with X-Rays. To evaluate the ability of the NCs to emit light upon excitation with X-Rays, a specific setup in a Micro-CT device has first been used (Fig. S6). This setup allows to irradiate the sample with various X-Rays energies and record the emitted light with an optical camera. For comparison, two compositions $Gd_{0.90}Tb_{0.10}F_3$ and $Gd_{0.80}Tb_{0.20}F_3$ have been studied in suspension in water (0.5 M of lanthanides). The intensity of luminescence produced under X-Rays irradiation at different energies is detailed Fig 3A and Fig 3B.

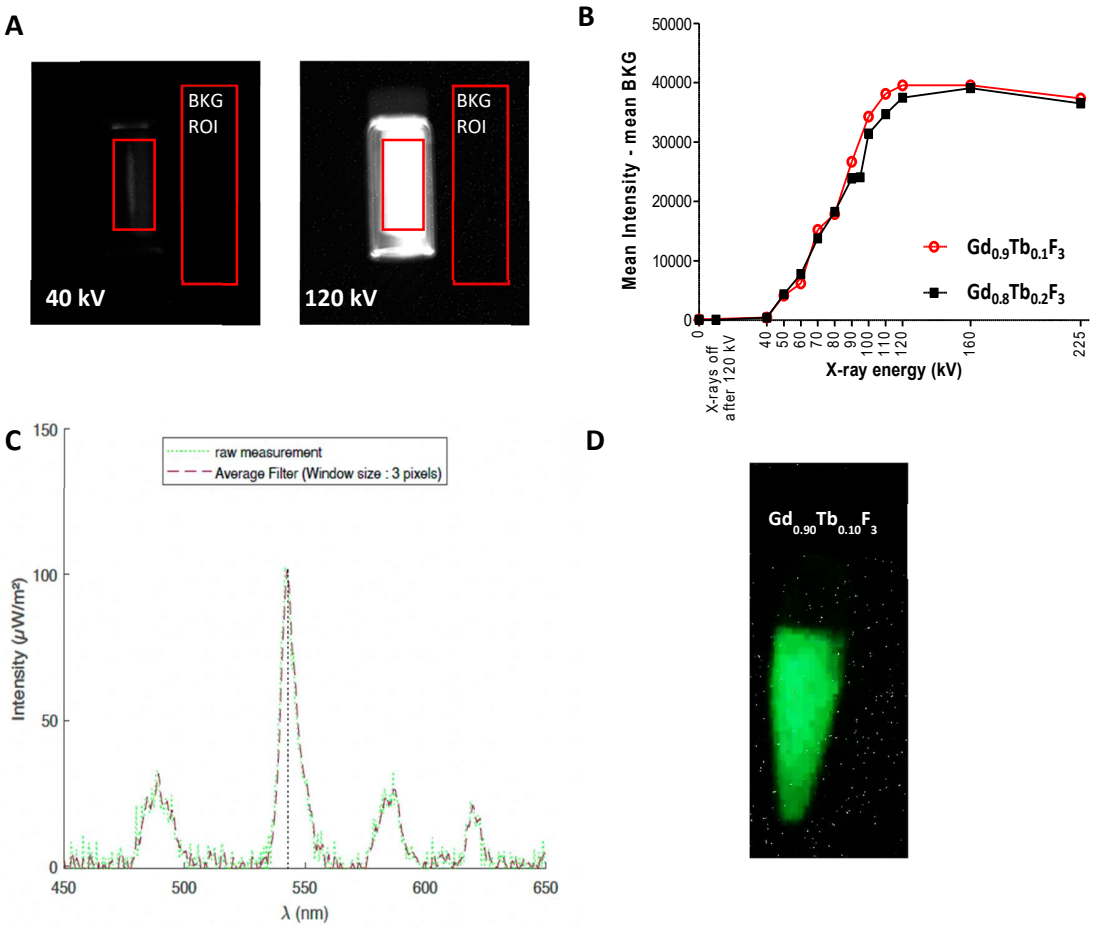

Fig. 3 A) Images of the tube containing the colloidal suspension of $Gd_{0.9}Tb_{0.1}F_3$ at various energies of X-Rays excitation (2,5 mA, Cu filter). Red areas correspond to ROI (luminescence and background - BKG) to determine the final intensity. **B)** Evolution of luminescence intensity as a function of the X-Rays energy of excitation. **C)** Emission spectra of colloidal suspension of $Gd_{0,9}Tb_{0,1}F_3$ in the Spectral photocount scanner at an energy of 120 kV and 300 mAs. **D)** Image of a tube containing an aqueous suspension of $Gd_{0,9}Tb_{0,1}F_3$ in water (0.5 M) submitted to X-Rays in the SPCCT.

Below 40 kV, no emission from the NCs is detected. For energies between 40 kV and 120 kV, the luminescence intensity increases with X-Rays energy following a linear behavior until reaching a plateau after 120 kV. At that point, the inorganic matrix of GdF_3 have absorbed the maximum of energy it could. The two compositions follow the same profile with a slightly higher intensity observed for $Gd_{0.90}Tb_{0.10}F_3$ in the 90-120 kV energy range. These results seem to agree with the experiments performed with UV excitation, although intensities measured with X-Rays are in the same margin of error.

Since the targeted application is the use of these systems as dual contrast agents with SPCCT, luminescence measurements have been performed on $Gd_{0.90}Tb_{0.10}F_3$ suspension in water with the spectral scanner (fig 3C and 3D). When submitted to X-Rays (120 kV, 300 mAs) a green light, specific to Tb^{3+}, is observed and imaged (fig 3D). The dedicated setup using an optical fiber (Fig S7) allows to

measure the spectra of the $Gd_{0.90}Tb_{0.10}F_3$ during excitation. These spectra present the four characteristic bands of Tb^{3+} luminescence centered at 488 nm, 543 nm, 582 nm and 619 nm (fig 3C). This result proves the ability of the NCs to generate visible light upon excitation with X-Rays from a clinical scanner.

Medical imaging with the NCs

After confirming the luminescence properties of these systems with X-Rays, their efficiency as contrast agent for CT imaging has been evaluated. Previous studies have shown the interest to use GdF_3 nanoparticles as a contrast agent for conventional CT imaging and K-edge imaging.[25,33] The composition with optimal luminescence properties $Gd_{0.90}Tb_{0.10}F_3$ was therefore studied to evaluate its ability to generate contrast. A range of suspensions with increasing concentrations of rare earths elements (0.015 M, 0.035 M, 0.1 M, 0.17M, 0.25M, 0,300 M) was placed in a dedicated phantom. The acquisition sequence was the same as generally used in conventional imaging for a patient (120 kVp and 200 mAs). Conventional and color K-edge CT imaging of the suspensions were performed in parallel to the quantification of the contrast agent concentration (Fig 4).

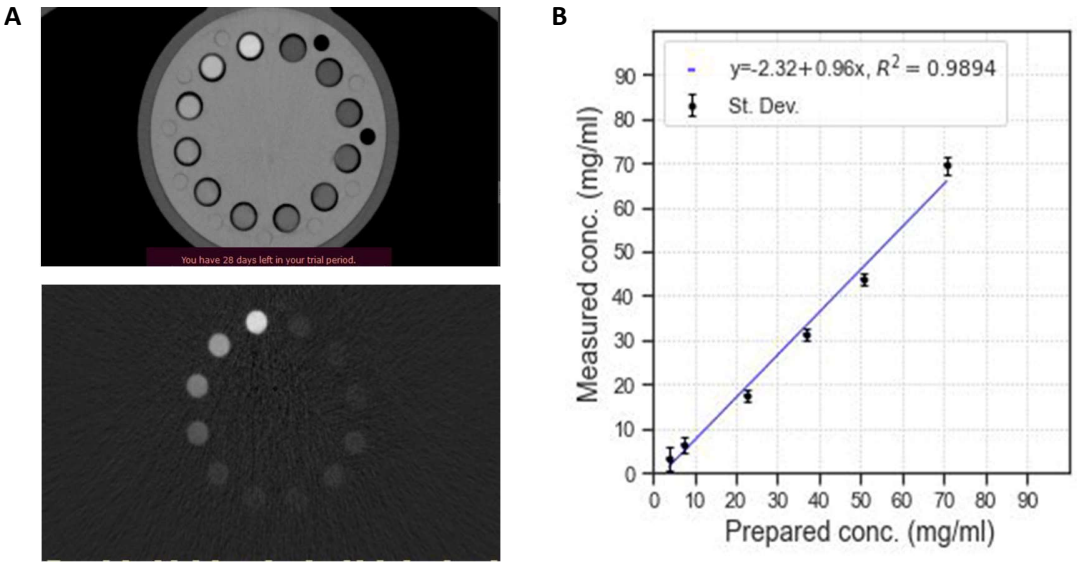

Fig. 4 Imaging and quantification studies on six suspensions of $Gd_{0.90}Tb_{0.10}F_3$ with concentration: 3.82 $mg.mL^{-1}$, 7.50 $mg.mL^{-1}$, 22.6 $mg.mL^{-1}$, 36.8 $mg.mL^{-1}$, 50.9 $mg.mL^{-1}$, 70.8 $mg.mL^{-1}$. A) Conventional CT imaging of a phantom containing the suspensions (up). Color K-edge imaging of the same phantom (down). The Gd concentration in the suspensions increases clockwise. B) Correlation between the gadolinium concentrations measured by ICP and by SPCCT.

With SPCCT, it is possible to do Conventional CT imaging as well as gadolinium-specific color K-edge imaging of the suspensions. Both imaging techniques show an increase of the contrast with the concentration of lanthanides. The $Gd_{0.90}Tb_{0.10}F_3$ NCs are well suited to be further used with this technology. Finally, the color K-edge imaging technique also allows to quantify the element inducing the contrast, through a direct correlation between the measured attenuation and the gadolinium concentration. Fig. 4 B) shows the linear correlation existing between the gadolinium concentration measured by SPCCT and the one measured by ICP. It becomes then possible accurately dose the quantity of contrast agent injected in vivo.

Surface functionalization of the $Gd_{0.90}Tb_{0.10}F_3$ NCs.

Surface functionalization of NCs was performed mainly following two approaches: i) Direct grafting of ligand on the surface or ii) design of core-shell system using a layer of silica (Scheme 1).

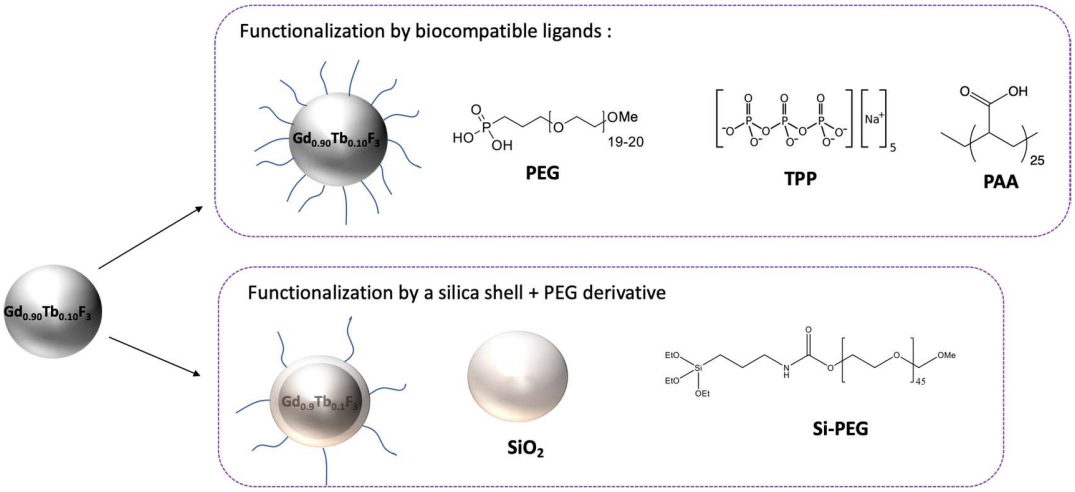

Scheme 1 General strategies for the design of surface-modified NCs and corresponding ligands.

The first strategy (ligand-based) is based on the stable anchoring of organic molecules (or macromolecules) through reactive functions (Phosphonates, phosphates, carboxylic acid) on the nanoparticles surface. The nature of the chemical bond formed between the nanoparticle and the molecule is coordinative, ionic or iono-covalent, conferring stability to the final system. Numerous works related to nanoparticles applications for in vivo studies have shown that high biocompatibility is achieved with polyethylene glycol (PEG) ligands. Following this general idea and based on previous work,[25] the studies have been focused on the use of phosphonic acid derived **PEG** (PPEG1000), which is known to have strong interactions with rare earth fluoride nanoparticles surface. The choice of **TPP**

(sodium tripolyphosphate) was motivated by the presence of multiple P=O and P-OH functions leading to strong anchoring on the nanoparticles surface and creating highly stable systems. Polyacrylic acid (**PAA**) is a polymer bearing several carboxylic functional groups along its structure which is expected to increase grafting stability.[37,38] As opposed to direct grafting, the core-shell design is indeed a two-step approach were the nanoparticles are first covered by a layer of silica followed by the covalent linking of a **Si-PEG** functionalized with a silane function (C-Si-O-Si bonding).

Efficient grafting of the various ligands on $Gd_{0.90}Tb_{0.10}F_3$ NCs was evidenced by FTIR (Fig S8). For TPP and PEG modifications, the intense signal around 1060 cm^{-1} is attributed to P-O stretching.[39] In the case of PAA modified NPs, the strong peak at 1680 cm^{-1} is attributed to C=O stretching of the carboxylic acid function. Core shell systems SiO_2@PEG, show the characteristic signal of Si-O-Si stretching overlapped with C-O-C stretching in the 1100 cm^{-1} region.[40,41] For all surface modifications involving organic moieties (SiO_2@PEG, PEG, and PAA) the presence of a signal in the 2850-2900 cm^{-1} area (C-H stretching) is observed.

HRTEM observations of the different surface-modified systems show no modification in terms of morphology nor crystallinity of the NCs cores (Fig. S9) with an average gyration diameter of 9.8 ± 0.8 nm. The NCs in suspension at pH = 7 have been analyzed by DLS and zeta potential measurements (table 2).

Table 2 Hydrodynamic diameter (Dh), zeta potential (ZP) and polydispersity index (PDI) of the various surface-modified NCs measured in water at pH= 6.

	Dh (nm)	*ZP (mV)*	*PDI*
$Gd_{0.90}Tb_{0.10}F_3$	13 ± 3	+ 48 ± 5	0.11
$Gd_{0.90}Tb_{0.10}F_3$@TPP	13 ± 3	- 45 ± 5	0.10
$Gd_{0.90}Tb_{0.10}F_3$@PEG	24 ± 3	+ 27 ± 5	0.15
$Gd_{0.90}Tb_{0.10}F_3$@PAA	24 ± 3	- 51 ± 5	0.14
$Gd_{0.90}Tb_{0.10}F_3$@SiO2@PEG	32 ± 3	- 25 ± 5	0.15

For all the systems considered, a clear increase of the Dh is observed after surface modification which is in agreement with the presence of the ligands on the NCs surface. The small Dh (13 nm) observed for $Gd_{0.90}Tb_{0.10}F_3$@TPP is consistent with the grafting of small molecules as opposed to polymers such as

PEG, PAA or SiO_2-PEG. The low polydispersity indexes indicate that the systems are homogenous, without the presence of aggregates at macroscopic scale. For all cases, the high absolute value of ZP (above 25 mV) confirms the high colloidal stability. The negative values measured for TPP, PAA, and SiO_2-PEG modifications respectively indicates the presence of negatively charged phosphonate, carboxylate and silanolate groups.

Finally, the quantification of the ligands was assessed with Thermogravimetric Analysis (TGA). All samples show mass loss in the 250°C-400°C range attributed to decomposition of the organic moieties. As expected in the case of the inorganic ligand TPP, no loss was observed. The results obtained for the various systems are summarized in Table 3.

Table 3 Mass loss determined from TGA analysis and corresponding calculated amount of ligand on each NCs.

Composition	*Total Organic mass loss (%)*	*Calculated numbers of Ligands per NCs*
$Gd_{0.90}Tb_{0.10}F_3$	- 6.4	2.58×10^3
$Gd_{0.90}Tb_{0.10}F_3$@TPP	none	none
$Gd_{0.90}Tb_{0.10}F_3$@PEG	- 40.3	2.61×10^3
$Gd_{0.90}Tb_{0.10}F_3$@PAA	- 21.8	5.44×10^3
$Gd_{0.90}Tb_{0.10}F_3$@SiO_2@PEG	- 12.8	2.68×10^2

The analysis performed on unmodified NCs shows a mass loss of 6.4 %. This result agrees with FTIR analysis (Fig. S8) and the presence of organic molecules (2-pyrrolidinone) on the surface. In the case of $Gd_{0.90}Tb_{0.10}F_3$@TPP no mass loss except the one corresponding to water was observed which is expected since no organic molecules are attached to the surface of the NCs. For the other systems the calculated number of ligands per nanoparticles are in the same order of magnitude. In the case of $Gd_{0.90}Tb_{0.10}F_3$@SiO_2@PEG, the number of organic ligands per nanoparticles is lower. Indeed, the reactivity of the surface of the NPs is driven by the interactions between the alkoxysilane-derived PEG and the active sites (silanols) on the silica layer. Since the number of silanols is limited, the total amount of grafted ligands is lower than in the case of a direct grafting on the $Gd_{0.90}Tb_{0.10}F_3$ with other macromolecules.

Effect of the ligands on the optical properties of the NCs

The influence of the various ligands or layer on the emission properties of the NCs has been studied. For a more detailed comparison, the $Gd_{0.9}Tb_{0.1}F_3$ nanoparticles were subjected to a surface cleaning procedure in order to remove the pyrrolidinone molecules from the surface. The efficiency of this cleaning step was controlled with TEM and XRD to make sure no evolution of the size nor the crystallinity of the NCs was observed and with FTIR to verify that no organic moieties were remaining on the surface of the nanoparticles (Fig S10). The luminescence properties have been recorded for all samples with the same concentration (0.06 M in lanthanides) in water and in D_2O, under UV excitation at 273 nm (fig. 5).

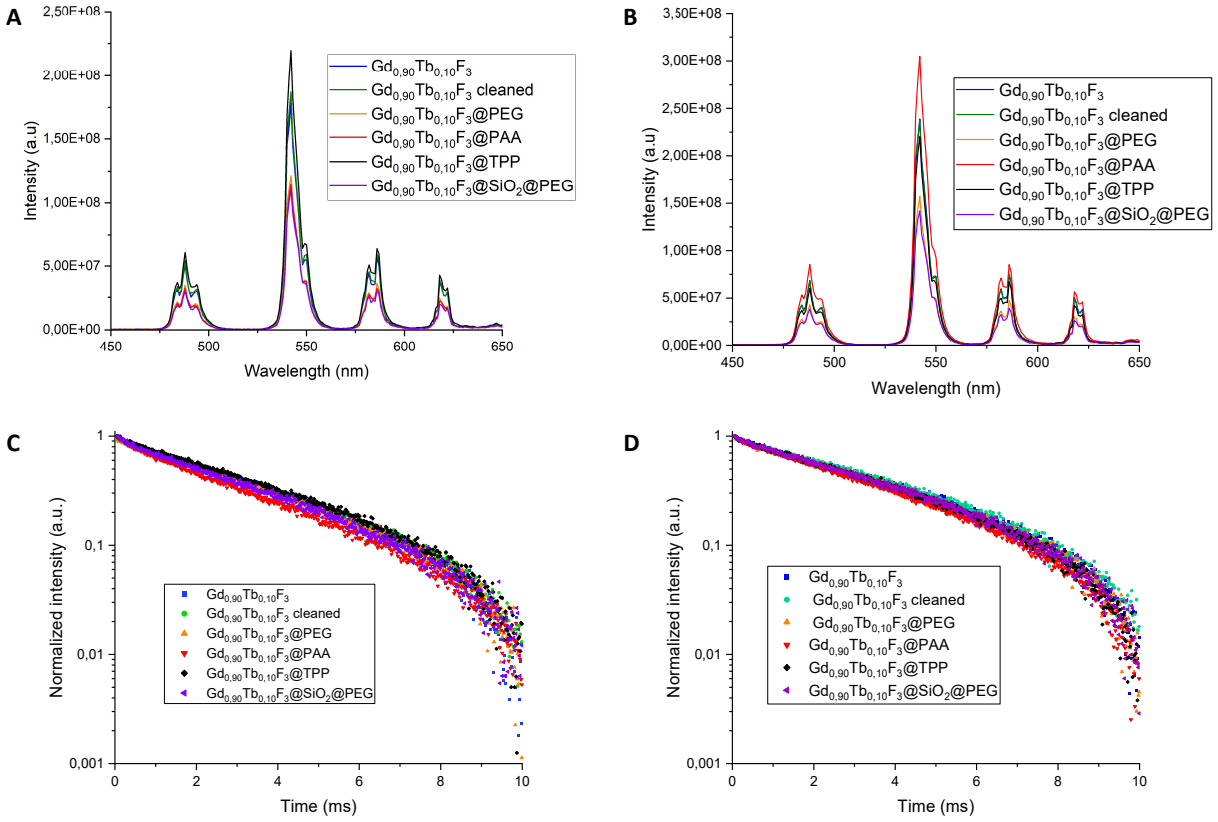

Fig. 5 A) *Luminescence spectra of the various surface-modified $Gd_{0,9}Tb_{0,1}F_3$ systems in H_2O, with excitation at 273 nm* **B)** *Luminescence spectra of the various surface-modified $Gd_{0,9}Tb_{0,1}F_3$ systems in D_2O, with excitation at 273 nm.* **C)** *Lifetime decay of colloidal suspension of $Gd_{0,9}Tb_{0,1}F_3$ systems in H_2O.* **D)** *Lifetime decay of colloidal suspension of $Gd_{0,9}Tb_{0,1}F_3$ systems in D_2O*

For all cases, the typical luminescence spectra of Tb^{3+} are observed with $^5D_4$ to ^7F_J (J = 6,5,4,3)

transitions. The luminescence intensities measured in water show the impact of the surface modification from clean ($Gd_{0.9}Tb_{0.1}F_3$) to functionalized NCs ($Gd_{0.9}Tb_{0.1}F_3$, $Gd_{0.9}Tb_{0.1}F_3$@PEG and $Gd_{0.9}Tb_{0.1}F_3$@SiO_2@PEG) with a decrease of the emission properties. This result can be explained by the presence of vibrators (O-H and N-H) in the molecules on the surface, acting as quenchers of the luminescence.[42] Interestingly in the case of $Gd_{0.9}Tb_{0.1}F_3$@TPP the measured intensity is the highest. The same experiments were conducted in D_2O and the luminescence intensity is higher than in the case of experiments performed in H_2O. This result confirms the luminescence quenching of excited Tb^{3+} by high-energy O–H vibrational modes.[43] The general trend remains the same with higher intensities in the case of unmodified NCs. The lowest variation is observed with $Gd_{0.9}Tb_{0.1}F_3$@TPP suggesting that the TPP acts as protective layer from the surroundings of the nanoparticles. Therefore, almost no variations are observed between H_2O or D_2O environments. On the contrary, $Gd_{0.9}Tb_{0.1}F_3$@PAA shows a much higher luminescence intensity in D_2O than in water. In that case, the carboxylic functions are deprotonated (confirmed by negative ZP measurements Table 3) meaning that the quenching of luminescence could only come from water entrapped in the grafted polymer layer (H-bonding) near the surface of the NCs. This study was completed by measurements of the luminescence lifetime at 543 nm after excitation at 273 nm in water and in D_2O (Table 4).

Table 4 Luminescence lifetime of each composition at 543 nm with an excitation wavelength of 273 nm and a concentration of 0.06 M in water and in D_2O.

Composition	*Lifetime (ms)*	*Lifetime (ms)*	*Correlation coefficient*
$Gd_{0.90}Tb_{0.10}F_3$	4.84 ± 0.03	5.56 ± 0.03	0.997
$Gd_{0.90}Tb_{0.10}F_3$ Cleaned	5.16 ± 0.03	5.82 ± 0.03	0.997
$Gd_{0.90}Tb_{0.10}F_3$@TPP	5.05 ± 0.04	5.10 ± 0.04	0.997
$Gd_{0.90}Tb_{0.10}F_3$@PEG	4.81 ± 0.03	5.47 ± 0.03	0.997
$Gd_{0.90}Tb_{0.10}F_3$@PAA	3.65 ± 0.03	4.50 ± 0.03	0.997
$Gd_{0.90}Tb_{0.10}F_3$@SiO_2@PEG	4.59 ± 0.03	5.11 ± 0.03	0.997

Whatever the solvent, the fluorescence lifetime measurement is higher for $Gd_{0.9}Tb_{0.1}F_3$ cleaned, confirming the effect of water but also the impact of the O-H and N-H oscillators from the ligands. In the cases of $Gd_{0.9}Tb_{0.1}F_3$@PEG, $Gd_{0.9}Tb_{0.1}F_3$@SiO_2@PEG and $Gd_{0.9}Tb_{0.1}F_3$ lifetimes are in the same range

with an increase by roughly 0,6 ms for all the systems when shifting from water to D_2O. Whatever the solvent, the lowest fluorescence lifetime is measured with $Gd_{0.9}Tb_{0.1}F_3$@PAA but with the highest variation from water to D_2O (0,85 ms). This confirms the previous measurements with the presence of water entrapped in the polymer layer. All the obtained results show that quenching of the luminescence has two origins, on one side, the presence of the ligands or layer on the surface of the NCs with O-H or N-H vibrators, on the other side, the presence of water more or less attracted/adsorbed at the surface of the NCs.

Finally, the low variation measured for $Gd_{0.9}Tb_{0.1}F_3$@TPP (0,05 ms) agrees with the observations of luminescence spectra and the protective activity of the inorganic TPP layer at the surface of the NPs. Unfortunately, despite many efforts, the stability of $Gd_{0.9}Tb_{0.1}F_3$@TPP decreased strongly when trying to increase the concentration in water or physiological serum. Being unable to reach values above 0.1 M the composition was not further evaluated with X-Rays activation.

Effect of ligands on the X-Rays activated luminescence properties of the functionalized NCs

In the previous part results showed that the various ligands grafted on the surface of the $Gd_{0.9}Tb_{0.1}F_3$ NCs played an essential role in the final optical properties of the systems when excited in the UV. The same approach was considered with the two different types of X-Rays activations: micro CT and SPCCT, on colloidal suspensions in water (0.5M) (Fig. 6).

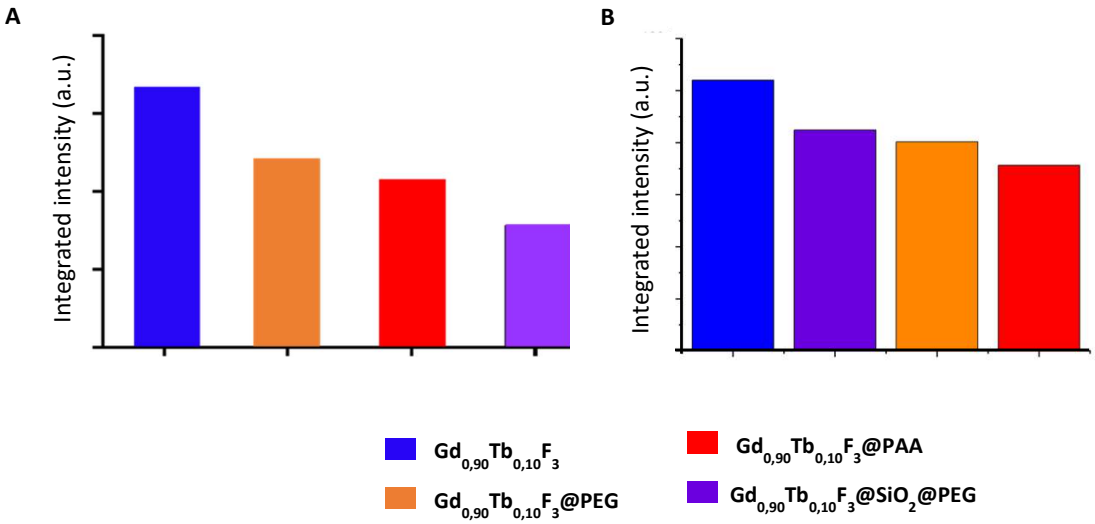

Fig. 6 A) Integrated luminescence intensities of various systems studied under X-rays excitation with micro CT (2,5 mAs, 120 kV). **B)** Integrated luminescence intensities of same systems under X-rays excitation of SPCCT (300 mAs, 120 kV).

Fig. 6 shows that the luminescence intensity of the nanoparticles is lower with the presence of the ligands on their surface independently of the X-Rays excitation values considered (2.5 mAs and 300 mAs) and as observed in the case of photoexcitation.

In the case of experiments conducted in micro-CT, the integrated intensity of the functionalized NCs follows the same trend as observed with UV excitation i.e. the intensity decreases as follow $Gd_{0.90}Tb_{0.10}F_3$@PEG > $Gd_{0.90}Tb_{0.10}F_3$@PAA > $Gd_{0.90}Tb_{0.10}F_3$@SiO_2@PEG. This last system seems to show properties well below the two others. Interestingly slight differences are observed when measurements are conducted with SPCCT, in that case the integrated intensities follow the order $Gd_{0.90}Tb_{0.10}F_3$@SiO_2@PEG > $Gd_{0.90}Tb_{0.10}F_3$@PEG > $Gd_{0.90}Tb_{0.10}F_3$@PAA with low differences. These discrepancies observed between micro CT and SPCCT can be explained by the type of setup used for the measurements. Indeed, micro CT experiments are very sensitive to the scattering of the nanoparticles and since $Gd_{0.90}Tb_{0.10}F_3$@SiO_2@PEG have the highest Dh (Table 3) with a surrounding silica shell, they have the strongest scattering. Therefore, the overall measured luminescence intensity is impaired by this phenomenon. In the case of SPCCT experiments, the optical fiber is directly immersed within the colloidal suspensions, therefore the scattering effect is limited and the signals are less perturbed during detection. Thus, the two PEGylated systems $Gd_{0.90}Tb_{0.10}F_3$@PEG and $Gd_{0.90}Tb_{0.10}F_3$@SiO_2@PEG seem to be the most promising for X-Rays triggered luminescence with SPCCT.

Functionalized NCs as contrast agents with CT scanner and SPCCT

To prove that functionalized NCs can be used as contrast agent for scanner imaging, conventionnal CT scanner and color K-edge imaging have been conducted with SPCCT. A phantom containing suspensions of functionalized NCs in Eppendorf (0.5 M in water) has been irradiated under 100 mAs, 120 keV using X-Rays of SPCCT (fig 7).

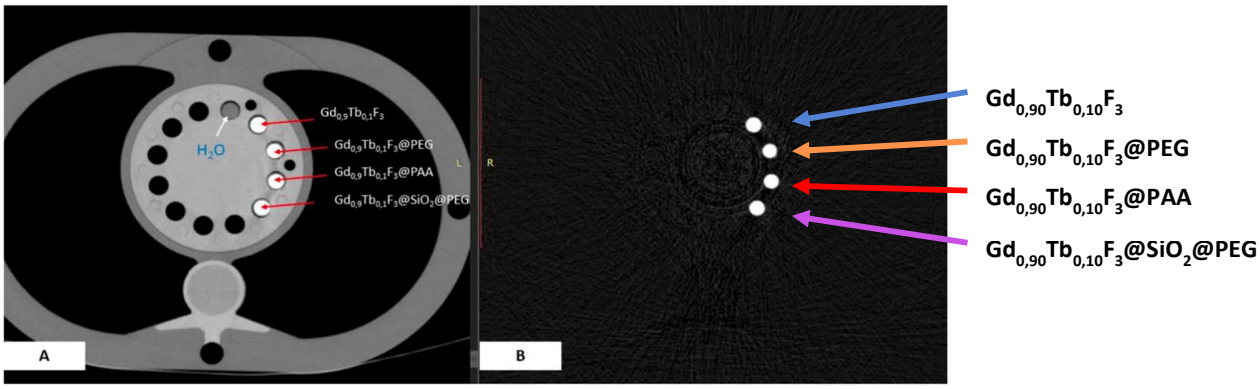

Fig. 7 A) *Conventional SPCCT imaging of a phantom containing colloidal suspensions of normal, PEG modified, PAA modified and SiO2@PEG modified NCs in water (0,5 M).* **B)** *Same phantom with color gadolinium k-edge imaging using SPCCT.*

The comparison to water sample confirms that functionalized NCs exhibits properties to generate high contrast in conventional SPCCT imaging. Color K-edge observations only show the signal of gadolinium and confirms that these samples are suitable for this technique of imaging (high contrast). The contrast being the same for all samples with K-edge imaging, we can also confirm that the concentration in gadolinium in the different suspensions is the same. Finally, whatever the ligand or coating, contrast was the same proving that the surface modification did not impair the NCs.

Proof of concept of in vivo dual imaging with SPCCT

To assess the ability of the NCs to be used as X-Rays based multimodal contrast agents in vivo, a study was carried out on a nude and healthy mouse with an acquisition sequence in the SPCCT. A suspension of $Gd_{0.90}Tb_{0.10}F_3$@PEG (50µL, 1M in physiological serum) was injected subcutaneously near the caudal thigh muscles of the anesthetized animal. Conventional CT, color gadolinium specific K-edge and luminescence imaging were then achived with the SPCCT (fig. 8).

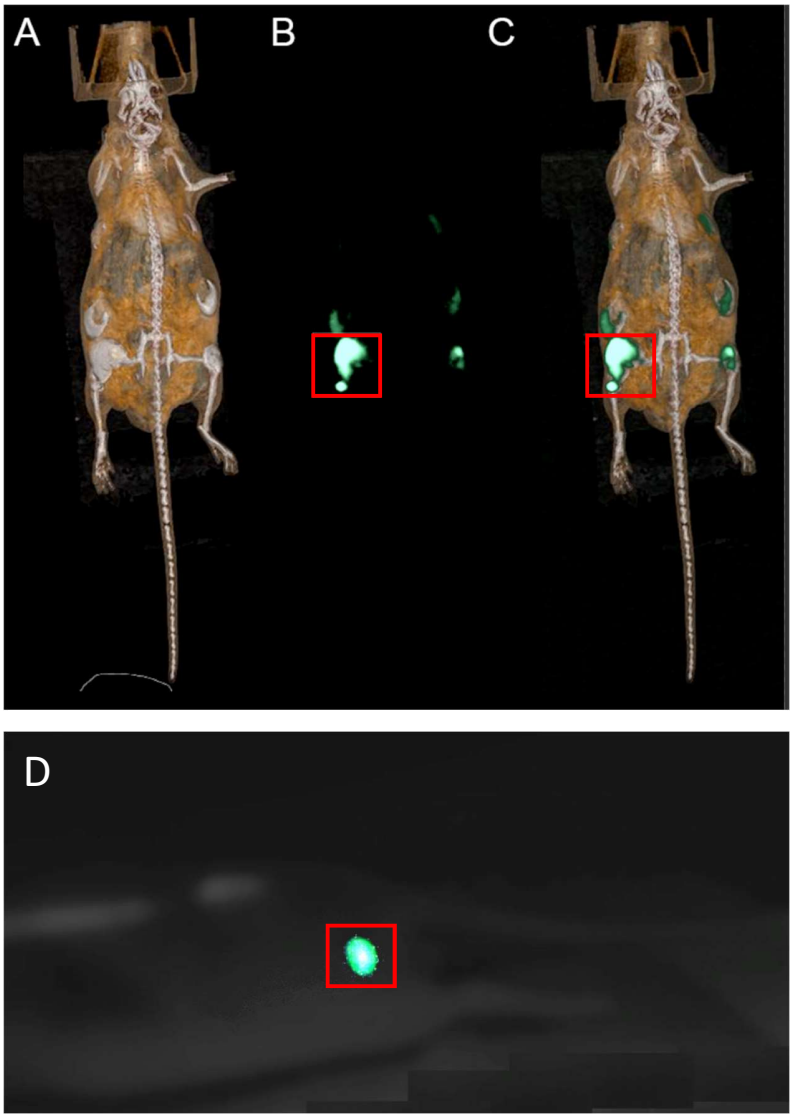

Fig. 8 Multimodal in vivo SPCCT imaging of the mouse 20 min after injection of $Gd_{0.90}Tb_{0.10}F_3$ in different sub-cutaneous sites at different volume and concentration. The area of interest (injection of the 1M suspension) is delimited by the red box. **A)** Conventional CT imaging of the whole animal. **B)** Color gadolinium specific K-edge imaging. **C)** Fusion of conventional and color K-edge. **D)** Luminescence imaging during acquisition with SPCCT.

While conventional CT imaging is providing a nonspecific imaging of the contrast agent (Fig. 8A), color K-edge imaging enables a specific and quantitative imaging of its biodistribution (Fig. 8B). Fusion of conventional and color K-edge imaging enables a comprehensive imaging of the contrast agent biodistribution (Fig. 8C). Monitoring was carried out over a period of 1 hour in order to follow the distribution of the nanoparticles. The systems remain localized and no diffusion in the surrounding tissues was observed. Finally, 24 hours after injection, the mouse showed no sign of infection. The

detection of the luminescence of NCs in vivo was conducted during a new acquisition sequence of the SPCCT, on the same animal, using the previously used parameters (120KeV – 300 mAs). Observations were made by camera during the X-Rays irradiation (fig 8 D). A clear and intense luminescence in the green at the injection site of the 1M suspension is observed. The signal is strong enough to be detected through the skin of the animal with the naked eye. The impact of the X-rays dose delivered for optimized imaging and the influence of the concentration of the particles is currently being studied and will be the subject of an upcoming paper.

Conclusions

In summary, we have successfully developed highly-efficient X-Rays activated nanoprobes for multimodal imaging. The nanocrystals consist in GdF_3 matrix doped with various ratios of Tb^{3+}. After finding the optimal composition of the original NCs with a systematic luminescence study, we were able to effectively evaluate the contrast capability in CT and SPCCT with gadolinium specific color K-edge imaging. The influence of surface modification on the luminescence properties was evaluated. Various strategies were considered using encapsulation with silica layer and direct grafting of molecules such as PEG, PAA or TPP derivatives. As the contrast with conventional CT and color K-edge imaging using SPCCT did not change, the luminescence intensity of these NCs in water was reduced compared to the original NCs. This was attributed to the quenching caused by surface ligands and water molecules. Our results suggest that the surface modified NCs are promising contrast agent for multimodal medical imaging with X-ray optical imaging, as well as for CT and SPCCT. The proof of concept performed on nude mice with SPCCT confirmed that the luminescence could be observed though the skin of the animal, together with strong contrast in CT and SPCCT.

Author Contributions

LC investigation, visualization, writing original draft; PA investigation; AG investigation, writing original draft; AH investigation, validation; FC investigation, methodology; AY investigation; LD conceptualization; PL conceptualization; SK investigation, writing original draft; SP conceptualization; JBL investigation; YY investigation; SAS-M conceptualization, writing original draft; BM conceptualization, writing original draft; PD conceptualization; FL conceptualization, supervision, writing original draft, writing review and editing.

Acknowledgements

This work was done in the frame of the SCANnTREAT project, this project has received funding from the European Union's Horizon 2020 research and innovation program under grant agreement N° 899549. Luminescence studies with SPCCT were funded by a public grant from the French National Research Agency (ANR) under the "France 2030" investment plan, which has the reference EUR MANUTECH SLEIGHT - ANR-17-EURE-0026. This work was funded by LABEX PRIMES (ANR-11-LABX-0063) of Université de Lyon, within the program "Investissements d'Avenir" (ANR-11-IDEX-0007), operated by the French National Research Agency (ANR). The experiments were based upon work done on the ISO 9001:2015 PILoT facility.

References

1 D. Bobo, K.J. Robinson, J. Islam, K.J. Turecht, S.R. Corrie, *Pharm. Res.,* 2016, **33**, 2373–2387.

2 S.D. Rawson, J. Maksimcuka, P.J. Withers, S.H. Cartmell, *BMC Biology*, 2020, **18**, 21.

3 J. F. Hainfeld, D. N. Slatkin, T. M. Focella and H. M. Smilowitz, *Br. J. Radiol.*, 2006, **79**, 248–253.

4 S. Si-Mohamed, D. Bar-Ness, M. Sigovan, D. P. Cormode, P. Coulon, E. Coche, A. Vlassenbroek, G. Normand, L. Boussel and P. Douek, *Nucl. Instrum. Methods Phys. Res. Sect. Accel. Spectrometers Detect. Assoc. Equip.*, 2017, **873**, 27–35.

5 S. Si-Mohamed, D. P. Cormode, D. Bar-Ness, M. Sigovan, P. C. Naha, J.-B. Langlois, L. Chalabreysse, P. Coulon, I. Blevis, E. Roessl, K. Erhard, L. Boussel and P. Douek, *Nanoscale*, 2017, **9**, 18246–18257.

6 S. A. Si-Mohamed, M. Sigovan, J. C. Hsu, V. Tatard-Leitman, L. Chalabreysse, P. C. Naha, T. Garrivier, R. Dessouky, M. Carnaru, L. Boussel, D. P. Cormode and P. C. Douek, *Radiology*, 2021, **300**, 98–107.

7 A. de Vries, E. Roessl, E. Kneepkens, A. Thran, B. Brendel, G. Martens, R. Proska, K. Nicolay, H. Grüll, *Invest. Radiol.*, 2015, **50**, 297–304.

8 J. Greffier, N. Villani, D. Defez, D. Dabli and S. Si-Mohamed, *Diagn. Interv. Imaging*, 2023, **104**, 167–177.

6 A. Pourmorteza, R. Symons, V. Sandfort, M. Mallek, M.K. Fuld, G. Henderson, E.C. Jones, A.A. Malayeri, L.R. Folio, D.A. Bluemke, *Radiology*, 2016, **279**, 239–245.

7 I. Blevis, in *Radiation Detectors for Medical Imaging,* ed. J.S. Iwanczyk, CRC Press, Boca Raton, first edn, 2015, ch. 3, pp. 169–192.

8 S. Si-Mohamed, D.P. Cormode, D. Bar-Ness, M. Sigovan, P.C. Naha, J.B. Langlois, L. Chalabreysse, P. Coulon, I. Blevis, E. Roessl, K. Erhard, L. Boussel, P. Douek, *Nanoscale*, 2017, **46**, 18246–18257

9 L. Sudheendra, G.K. Das, C. Li, D. Stark, J. Cena, S. Cherry, I.M. Kennedy, *Chem. Mater.*, 2014, **26**, 1881−1888.

10 L. Song, X. H. Lin, X. R. Song, S. Chen, X. F. Chen, J. Li and H. H.Yang, *Nanoscale*, 2017, 9, 2718-2722.

11 H. Chen, D. C. Colvin, B. Qi, T. Moore, J. He, O. T. Mefford, F. Alexis, J. C. Gore and J. N. Anker, *J. Mater. Chem.*, 2012, **22**, 12802-12809.

12 J.C. Hsu, L.M. Nieves, O. Betzer, T. Sadan, P.B. Noël, R. Popovtzer, D.P. Cormode, *Wiley Interdiscip. Rev. Nanomed. Nanobiotechnol.*, 2020, **12**, e1642.

13 Z. Hong, Z. Chen, Q. Chen and H. Yang, *Acc. Chem. Res.*, 2023, **56**, 37−51.

14 D. P Cormode, S. Si-Mohamed, D. Bar-Ness, M. Sigovan, P.C. Naha, J. Balegamire, F. Lavenne, P. Coulon, E. Roessl, M. Bartels, M. Rokni, I. Blevis, L. Boussel, P. Douek, *Sci. Rep.*, 2017, **1**, 4784.

15 L. Song, X.H. Lin, X.R. Song, S. Chen, X.F. Chen, J. Li, H.H. Yang, *Nanoscale*, 2017, **9**, 2718−2722.

16 X. Li, Z. Xue, M. Jiang, Y. Li, S. Zeng, H. Liu, *Nanoscale*, 2018, **10**, 342−350.

17 T. Guo, Y. Lin, W.J. Zhang, J.S. Hong, R.H. Lin, X.P. Wu, J. Li, C.H. Lu and H.H. Yang, *Nanoscale*, 2018, **10**, 1607-1612.

18 Q. Ju, S. Luo, C. Chen, Z. Fang, S. Gao, G. Chen, X. Chen and N. Gu, *Adv. Healthcare Mater.*, 2019, **8**, 1801324.

19 Z.Z. Chen, L.C. Wang, D. Manoharan, C.L. Lee, L.C. Wu, W.T. Huang, E.Y. Huang, C.H. Su, H.S. Sheu, C.S. Yeh, *Adv. Mater.*, 2019, **31**, 1905087.

20 H. Lusic, M. W. Grinstaff, *Chem. Rev.*, 2013, **113**, 1641-1666.

21 E. Hemmer, N. Venkatachalam, H. Hyodo, A. Hattori, Y. Ebina, H. Kishimotoac and K. Soga, *Nanoscale*, 2013, **5**, 11339-11361.

22 S. Lahtinen, A. Lyytikäinen, H. Päkkilä, E. Hömppi, N. Perälä,M. Lastusaari and T. Soukka, *J. Phys. Chem. C*, 2016, **121**, 656-665.

23 D. Lisjak, O. Plohl, M. Ponikvar-Svet and B. Majaron, *RSC Adv.*, 2015, **5**, 27393-27397.

24 D. Lisjak, O. Plohl, J. Vidmar, B. Majaron and M. Ponikvar-Svet, *Langmuir*, 2016, **32**, 8222-8229.

25 N. Halttunen, F. Lerouge, F. Chaput, M. Vandamme, S. Karpati, S. Si-Mohamed, M. Sigovan, L. Boussel, E. Chereul, P. Douek and S. Parola, *Sci. Rep.*, 2019, **9**, 12090.

26 S. Si-Mohamed, A. Thivolet, P.-E. Bonnot, D. Bar-Ness, V. Képénékian, D. P. Cormode, P. Douek and P. Rousset, *Invest. Radiol.*, 2018, **53**, 629–639.

27 S. Si-Mohamed, D. Bar-Ness, M. Sigovan, V. Tatard-Leitman, D. P. Cormode, P. C. Naha, P. Coulon, L. Rascle, E. Roessl, M. Rokni, A. Altman, Y. Yagil, L. Boussel and P. Douek, *Eur. Radiol. Exp.*, 2018, **2**, 34.

28 H.K. Kim, G.H. Lee, Y. Chang, *Future Med. Chem.*, 2018, **10**, 639-661.

29 M. P. Menon and J. James, *J. Chem. Soc. Faraday Trans. 1 Phys. Chem. Condens. Phases*, 1989, **85**, 2683.

30 J.C.G. Bünzli and C. Piguet, *Chem. Soc. Rev.*, 2005, **34** , 1048 —1077.

31 H. Liu, C. T. Xu, D. Lindgren, H. Xie, D. Thomas, C. Gundlach and S. Andersson-Engels, *Nanoscale*, 2013, **5**, 4770-4775.

32 F. Mpambani, A. K. O. Åslund, F. Lerouge, S. Nyström, N. Reitan, E. M. Huuse, M. Widerøe, F. Chaput, C. Monnereau, C. Andraud, M. Lecouvey, S. Handrick, S. Prokop, F. L. Heppner, P. Nilsson, P. Hammarström, M. Lindgren and S. Parola, *ACS Appl. Bio Mater.*, 2018, **1**, 462-472.

33 S. Karpati, V. Hubert, I. Hristovska, F. Lerouge, F. Chaput, Y. Bretonnière, C. Andraud, A. Banyasz, G. Micouin, M. Monteil, M. Lecouvey, M. Mercey-Ressejac, A.K. Dey, P.N. Marche, M. Lindgren, O. Pascual, M. Wiar and S. Parola, Nanoscale, 2021, **13**, 3767-3781.

34 H. H. Caspers, S. A. Miller, H. E. Rast and J. L. Fry, *Phys. Rev.*, 1969, **180**, 329–333.

35 J.C.G. Bünzli and S. V. Eliseeva, in *Lanthanide Luminescence*, ed. P. Hänninen and H. Härmä, Springer, Heidelberg, 2010, ch. 7, pp. 1–45.

36 M.A. Omary, H.H. Patterson, in *Encyclopedia of Spectroscopy and Spectrometry*, ed. J.C. Lindon, G.E. Tranter, D.W. Koppenaal, Academic Press, third edn, 2017, pp. 636-653.

37 N. Liu, N. Gobeil, P. Evers, I. Gessner, E.M. Rodrigues and E. Hemmer, *Dalton Trans.*, 2020, **49**, 16204-16216.

38 S. Wilhelm, M. Kaiser, C. Wurth, J. Heiland, C. Carrillo-Carrion, V. Muhr, O. S. Wolfbeis, W. J. Parak, U. Resch-Genger and T. Hirsch, *Nanoscale*, 2015, **7**, 1403-1410.

39 L. Daasch and D. Smith, *Anal. Chem.*, 1951, **23**, 853–868.

40 A. Agarwal and M. Tomozawa, *J. Non-Cryst. Solids*, 1997, **209**, 166–174.

41 N. S. Vrandečić, M. Erceg, M. Jakić and I. Klarić, *Thermochim. Acta*, 2010, **498**, 71–80.

42 A. Beeby, I. M. Clarkson, R. S. Dickins, S. Faulkner, D. Parker, L. Royle, A. S. de Sousa, J. A. G. Williams and M. Woods, *J. Chem. Soc. Perkin Trans. 2*, 1999, 493–504.

43 J.-C. Boyer, F. Vetrone, L. A. Cuccia and J. A. Capobianco, *J. Am. Chem. Soc.*, 2006, **128**, 7444–7445.